Lawrence Berkeley National Laboratory

LBL Publications

Title

Flexible Electronics: Heat-Free Fabrication of Metallic Interconnects for Flexible/Wearable Devices (Adv. Funct. Mater. 40/2019)

Permalink

https://escholarship.org/uc/item/7248896k

Journal

Advanced Functional Materials, 29(40)

ISSN

1616-301X

Authors

Martin, Andrew
Chang, Boyce S
Martin, Zachariah
et al.

Publication Date

2019-10-01

DOI

10.1002/adfm.201970278

Peer reviewed

eScholarship.org Powered by the California Digital Library
University of California

ADVANCED FUNCTIONAL MATERIALS

www.afm-journal.de

Check for updates

Heat-Free Fabrication of Metallic Interconnects for Flexible/Wearable Devices

*Andrew Martin, Boyce S. Chang, Zachariah Martin, Dipak Paramanik, Christophe Frankiewicz, Souvik Kundu, Ian D. Tevis, and Martin Thuo**

Exploiting interfacial excess (Γ), Laplace pressure jump (ΔP), surface work, and coupling them to surface reactivity have led to the synthesis of undercooled metal particles. Metastability is maintained by a core–shell particle architecture. Fracture of the thin shell leads to solidification with concomitant sintering. Applying Scherer's constitutive model for load-driven viscous sintering on the undercooled particles implies that they can form conductive traces. Combining metastability to eliminate heat and robustness of viscous sintering, an array of conductive metallic traces can be prepared, leading to plethora of devices on various flexible and/or heat sensitive substrates. Besides mechanical sintering, chemical sintering can be performed, which negates the need of either heat or load. In the latter, connectivity is hypothesized to occur via a Frenkel's theory of sintering type mechanism. This work reports heat-free, ambient fabrication of metallic conductive interconnects and traces on all types of substrates.

1. Introduction

Fabrication of high-utility neoteric electronic devices often integrates different classes of materials to accommodate a multitude of functionalities. Complexity that arises from materials property mismatch (especially thermal expansivity) is often a major challenge to the fabrication of such devices.[1] Advances in flexible/wearable electronic devices and Internet of Things (IoT) exacerbates fabrication challenges largely due to thermal effects on the substrates and need to join smaller components. These demands have inspired an array of solutions, especially those geared toward component bonding. Colloids,[2] especially nanoparticles,[3] have been used in welding,[3d,4] soldering,[5] brazing,[6] and analogous processes.[7] Use of nanomaterials, however, does not circumvent fabrication challenges and, in some cases, may introduce new difficulties.[8]

Utilizing material surface properties, such as interfacial excess (Γ_i), surface tension (γ), and shear modulus (G), has inspired quantitative synthesis of undercooled liquid metal core–shell (ULMCS) particles through the so-called SLICE technique.[9] The synthesized core-shell architecture frustrates heterogeneous nucleation through a thin (≈<2 nm)[10] oxide shell that is polished in situ to form a smooth continuous surface. This delicate passivating oxide is further stabilized using felicitous choice of organic ligands. Solidification is effectively inhibited via a physical barrier to heterogeneous nucleants and a thermodynamic barrier to homogeneous nucleation (**Figure 1**a).

The ULMCS particles instantaneously solidify upon fracture of the shell.[11] Sintering, hence application of undercooled metal particles in fabrication of flexible or wearable devices, has, however, not been realized in part due to poor understanding of stress propagation across such particles. Sintering soft matter particles is constrained by substrate adhesion, particle size polydispersity, packing density and inclusion of rigid bodies. The latter can manifest as non-undercooled particles even with high (>97%) undercooling yield. We anticipate that ULMCS particles, like gels, sinter by flow[12] albeit with concomitant spontaneous phase change, spinodal decomposition and crystallization. Being non-Newtonian liquids, constitutive models for viscous sintering can inform pathways to circumvent some of the stated constraints. For example, understanding relation between densification and strain propagation, $\dot{\varepsilon}_x$, through Scherer's model (Equation (1)),[13] allows us to infer that application of plane stress leads to significantly higher densification rate ($\dot{\rho}$) than applying normal stress

$$\dot{\varepsilon}_x = \dot{\varepsilon}_f + \frac{1}{E}\left[\sigma_x + \upsilon\left(\sigma_y + \sigma_z\right)\right] \tag{1}$$

A. Martin, Dr. B. S. Chang, Dr. C. Frankiewicz, Prof. M. Thuo
Department of Materials Science and Engineering
Iowa State University
Ames, IA-50010, USA
E-mail: mthuo@iastate.edu

Z. Martin, Dr. D. Paramanik, Dr. I. D. Tevis
SAFI-Tech Inc.
Ames, IA-50011, USA

S. Kundu, Prof. M. Thuo
Department of Electrical and Computer Engineering
Iowa State University
Ames, IA-50010, USA

Prof. M. Thuo
Microelectronics Research Center
Iowa State University
Ames, IA-50010, USA

Prof. M. Thuo
Center for Crop Utilization Research
Iowa State University
Ames, IA-50010, USA

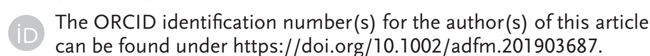
The ORCID identification number(s) for the author(s) of this article can be found under https://doi.org/10.1002/adfm.201903687.

DOI: 10.1002/adfm.201903687

© 2019 WILEY-VCH Verlag GmbH & Co. KGaA, Weinheim

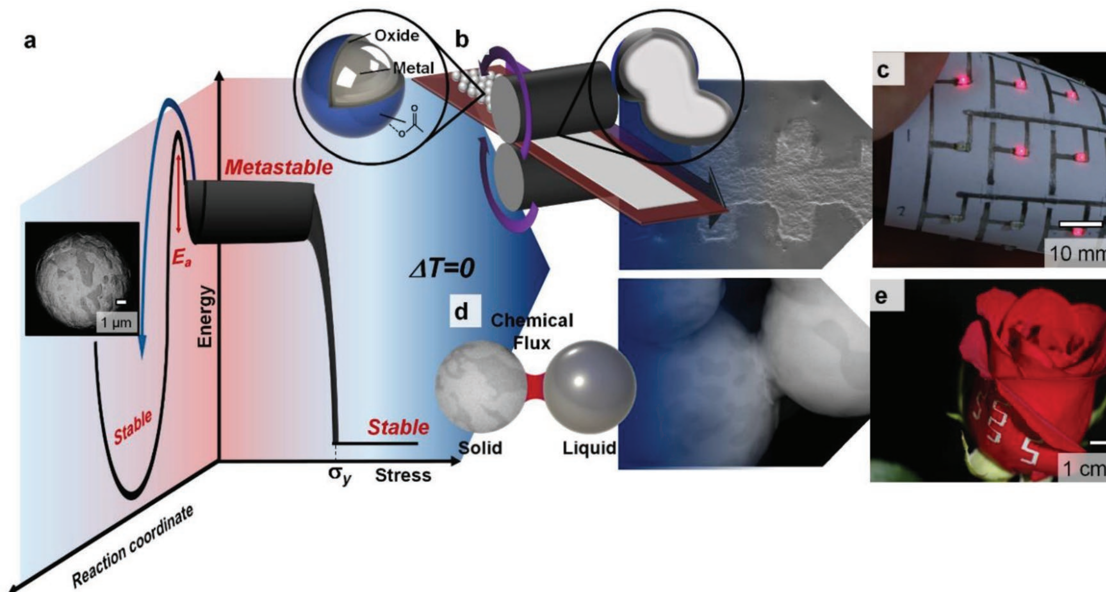

Figure 1. Schematic illustration of the heat-free manufacturing paradigm using metastable liquid metal particles. a) Orthogonal thermodynamic relaxation pathways of molten metal: the unrestricted path to stable solid metal with concomitant spinodal decomposition (insert on the left), the frustrated relaxation pathway (right) leads to a high energy, metastable state that relaxes upon application of b) mechanical or d) chemical stress. The former gives continuous solid films while the latter gives porous conductive films. c) Functional flexible display made using mechanical relaxation of undercooled metal particles. e) Printed conductive traces on the surface of a fragile superhydrophobic rose petal using chemical sintering.

where $\dot{\varepsilon}_x$ is the strain rate in the x-direction, $\dot{\varepsilon}_f$ is free strain, ν is the Poisson ratio, E is the elastic modulus, and σ is the applied stress. Free strain is related to densification, $\dot{\varepsilon}_f = \dot{\rho}/3\rho$. It also follows that under plane stress (e.g., on x–y plane), densification occurs much faster (≈24%) since it is related to contraction in a single (z-for stress on x–y) direction (Equation (2))[14]

$$\frac{\dot{\rho}}{\rho} = -\frac{\dot{\varepsilon}_f\,(1+\upsilon)}{(1-\upsilon)} \tag{2}$$

Coupling thermodynamic metastabilization and granular densification, we demonstrate applications of ULMCS particles for heat-free fabrication of mechanically robust, electrically conductive interconnections. We demonstrate ambient temperature molding, sheet rolling for continuous films (Figure 1b), and chemical sintering to create porous films (Figure 1d). Exploiting asymmetry in propagation of applied stresses across a bed of colloidal matter,[15] different structures are created under normal and shear stresses. Shear (plane) stress allows fabrication of uniform thin films (Figure 1b) which can be further advanced into fabricating conductive traces with tunable thickness on flexible substrates (Figure 1c). As expected, when normal stress is applied to a packed bed of ULMCS particles, surface deformations dominate, leading to asymmetric solidification, flow and surface sintering. Unique features of the ULMCS particles allow fabrication of conductive traces on otherwise unprecedented platforms (Figure 1e).

2. Results and Discussion

Undercooled metal particles were prepared using the SLICE method.[9b] Field‘s metal—a low-melting, fusible eutectic alloy of bismuth, indium, and tin (Bi: 32.5/In: 51/Sn: 16.5 wt%, T_m = 62 °C)—was significantly undercooled (degree of undercooling, $\Delta T/T_m$ = 0.34) at high yields (>97%, see Figure S1, Supporting Information). The as-prepared particles were stable at ambient conditions for >6 months (only ≈3% loss in undercooled particles over 6 months). The material is also stable against transportation-associated or ambient vibrations.

2.1. Mechanical Processing

To understand the impact of applied stress on the undercooled particles, we adopt models of stress propagation in granular matter (e.g., Equations (1) and (2)). In general, propagation of applied stress in a dry bed of colloids is dynamic and asymmetric over a small quasilinear subset of particles. Interparticle force law dictates that applied force has a power relation to particle compressibility ($f\ \alpha\ \delta$a where δ is particle compressibility and $a > 1$).[15] This ansatz manifests as an asymmetric response of the compressible undercooled metal particles to normal or shear stress, with the latter affecting the whole colloidal bed with concomitant rapid densification (Equation (2)). Applied normal stresses, as expected,[30] propagate through contact lines that project the stress toward the container walls which may lead to asymmetric densification.

To validate the ansatz, a bed of ULMCS particles on a flat surface was subjected to normal (σ_z) and shear (τ_{xy}) stresses (**Figure 2**a,f). As a control, capillary-driven packing of the particles (no externally applied mechanical stress) led to no sintering (Figure S2a, Supporting Information) but as expected, particles jam—akin to green body in ceramics. For a bilayer of the particles under normal stress, complete deformation of the topmost

 © 2019 WILEY-VCH Verlag GmbH & Co. KGaA, Weinheim

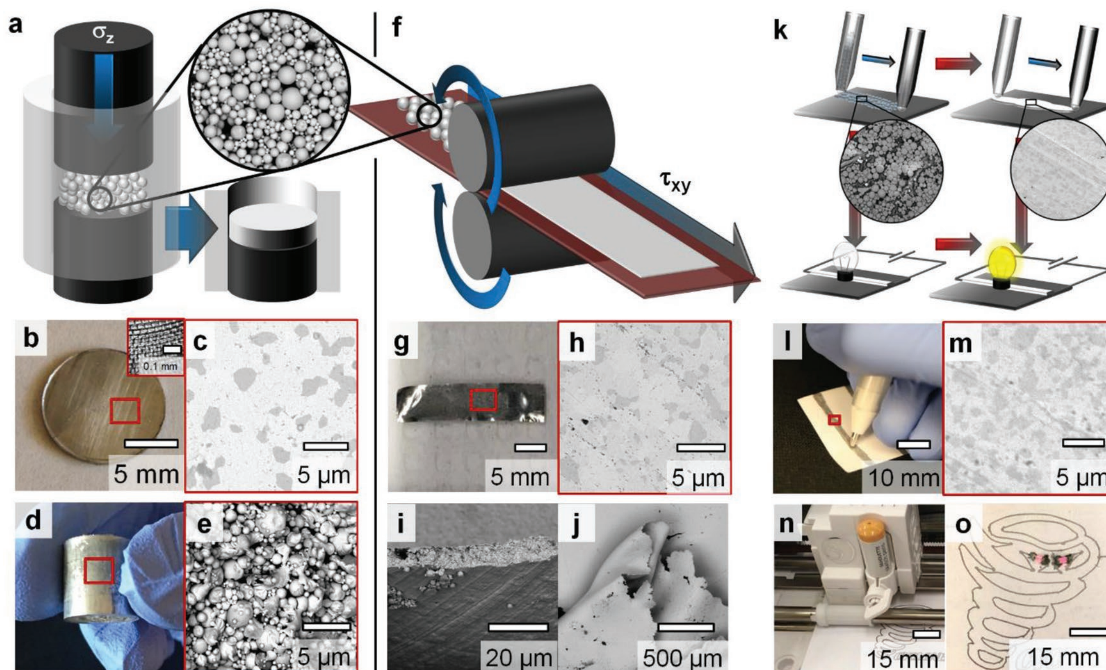

Figure 2. Mechanical processing of ULMCS particles. a) Effect of applied normal force on a traditional powder processing press to give b) a coin and d) a billet. Imprinted surface patterns on the coin are realized using a patterned die (inset). c) Spinodal decomposition occurs upon solidification (c). d) The billet shows asymmetric deformation as expected for interaction colloids with smooth continuous surfaces but e) granulated core. f–j) Applied shear stress (rolling) leads to thin flexible films with concomitant isolation of the few i) non-undercooled particles. k–o) Application of the mechanical activation in a two-step fabrication process for writing conductive traces on flexible substrates. Particles are deposited as an ink then activated with a blunt object to give conductive lines. Both l) manual and n) robotic writing can be used with comparable results. A 2D plotter is used to create a complex trace on which two LED lights glow upon connection to a power source.

layer occurred with concomitant, albeit weak, bonding to the slightly deformed bottom layer (Figure S2b, Supporting Information). When a thicker bed was used, asymmetric deformations occurred with significant reduction in the extent of deformation with depth. As expected, the formed structures depend on yield of undercooled particles as stress propagation in non-undercooled particles (nondeformable colloids under low σ_z) is significantly different than in the deformable undercooled analogs (Figure S2c–f, Supporting Information).[15] Using conventional powder processing (1000–1500 psi pressure), however, the ULMCS particles were molded into disks (Figure 2b and Figure S2g, Supporting Information) or pellets (Figure 2d). With a thicker particle bed, the effect of nonuniform stress propagation, as expected in deformable colloids,[15] leads to asymmetric sintering. Surface and sides of the so-pressed billets form continuous outer surfaces (Figure 2d) while the core is granulated (Figure 2e and Figure S2h, Supporting Information). Patterned dies, as expected, imprint the features on the surface (Insert Figure 2b and Figure S3, Supporting Information).

To evaluate the role of shear stress, we used a jeweler's roller (Figure S4a, Supporting Information) to convert ULMCS particles into thin metallic sheets (Figure 2f–j). The obtained films appear shiny akin to a metallic foil (Figure 2g) but contain defects (Figure 2h) upon closer inspection with SEM. Rolling induces complete flow and solidification of ULMCS particles albeit with integration of some of the surface oxide to create defects (Figure 2i). Despite the defects, large thin sheets can be fabricated with sheet resistances of 298 versus 52 µΩ cm for bulk Field's metal. Introducing a flux that dissolves the surface oxide significantly improves sheet resistance to almost that of the bulk metal (58 vs 52 µΩ cm). Adventitious spherical solid particles aggregate on the surface of the pressed film, and interestingly, they do not amalgamate with each other or the formed film (Figure 2j). We infer these to be the non-undercooled components with a passivating oxide that inhibits metal-metal bonding. These adventitious particles always rest at the edge of the sheet showing that the rolling process can also remove non-undercooled particles by pushing them toward the edge of the reflowing liquid. The Supporting Information contains further experimental details.

Based on observations above, fabrication of metals structures under no heat and at low mechanical stress is feasible. Borrowing from writing, a simple method of scribing interconnects is reported (Figure 2k).[16] An ink based on ULMCS particles suspended in hydroxyethyl cellulose (75 wt% metal) was formulated and used either manually (Figure 2l) or with a 2D plotter (Figure 2n). A pen with the formulated ink deposits the particles, while a blunt tip (e.g., a pen with no ink) serves as a roller. The spherical liquid particles deform into uniform films that are solid, continuous, and conductive (resistivity = 15 µΩ-cm). As expected, all solidification occurs with concomitant spinodal decomposition (Figure 2c,h,m).[9b]

 © 2019 WILEY-VCH Verlag GmbH & Co. KGaA, Weinheim

2.2. Chemical Sintering

Since a thin shell stabilizes the ULMCS particles, capillary self-assembly, with concomitant concentration of a dilute etchant, can lead to localized dissolution of the shell. This ansatz relies on felicitous choice of carrier-fluid evaporation conditions, fluid viscosity, and etchant concentration. At high etchant concentration, an accelerated, but localized, etching ensues leading to contact between two adjacent particles. This focused release of the undercooled liquid cascades throughout the particle bed leading to point (tangential) contacts and solidification. This process, therefore, entails Coalescence of Undercooled Particles through a Chemical Trigger (for brevity abbreviated as CUPACT). **Figure 3**a schematically captures the capillary-driven CUPACT process with a highlight of an undercooled and a solid particle. Since capillary forces are not strong enough to fracture the shell, CUPACT occurs with retention of sphericity (Figure 3b–d) after point soldering (Figure 3d). The CUPACT films had density, $\rho = 3.59$ g cm^{-3} (bulk 7.88 g cm^{-3}) suggesting ≈45% porosity (Figure 3b–c,e–g). The high porosity implies a lower thermal conductivity, $k = 8.61$ W m^{-1} K^{-1} versus bulk solid Field's metal (22.0 W m^{-1} K^{-1}). Initiating CUPACT on a substrate that can alloy with the ULMCS particles leads to anchoring of the sintered particle bed on the substrate (Figure 3f). Using a thin (≈450 nm) Au film on a silicon wafer as substrate, for example, leads to soldering of the particles onto the substrate (Figure 3e–g). In the case of surface soldering, an intermetallic interface forms with concomitant CUPACT of overlaying particles. Since CUPACT is concentration dependent, etchant concentration dictates properties of formed film (Figure 3h). With a more reactive etchant, like hydrochloric acid, film resistivity decreases faster with increasing acid concentration compared to dilute acetic acid, DLAA (Figure 3h).

The fully sintered CUPACT films had resistivity of 63 μΩ cm (with 60% DLAA) which is comparable to that of mechanically rolled films (58 μΩ cm) and sheet resistance of bulk Field's metal (52 μΩ cm). Since the materials have significant differences in densities, comparing specific properties (raw property/density), we note that the specific thermal conductivity of the bulk and CUPACT films is surprisingly similar (2.4×10^{-3} W m^2 g^{-1} K^{-1}) although slightly higher than that of the mechanically formed films (1.9×10^{-3} W m^2 g^{-1} K^{-1}). An Ashby plot comparing electrical resistance to density captures the novelty of these materials as different forms of the same material traversing across multiple elements (Figure 3i and Table S2, Supporting Information). More characterization details are given in the Supporting Information.

2.3. Application of Activated Particles in Printed Electronics

To enable rapid prototyping, we adopted the metal particle inks to screen-printing. Successful screen-printing relies on deposition under low shear stress without triggering solidification. We inferred that interparticle Hertzian interactions,[17] and associated hydrodynamics mediated elastic scattering of shear stress, in a colloidal suspension permits dispersion without mechanical fracture of the particles. Increased viscosity of the carrier fluid and stochastic (anisotropic) particle distribution renders faster and more isotropic energy absorption abetted by Stokes' drag and interparticle carrier fluid lubricity.[17] Since ULMCS particles have smooth deformable surfaces, high shear stresses are required to transfer stress into the particles due to surface roughness dependent elastic deformation limit,[18] hence high concentration of these particles can be used.

Based on understanding of stress propagation and deformation of interacting colloids, screen print of conductive lines via a two-step process (deposition then activation) was developed. We employed two types of screens from Novacentrix and Powerfilm. The former design (**Figure 4**a) is a standard to measure sheet resistance of screen-printed inks while the latter (Figure 4d) targets flexible solar cell contacts. Screen-printed lines show continuity (Figure 4b) with well-formed edges (Figure 4c). We demonstrate good resolution by printing elaborate traces with successful reproduction of features ≈240 μm (Figure 4e,f).

Electrical resistance of screen-printed designs, however, depends on activation method. For the conductive lines (Figure 4b), mechanical activation produced lower (25 Ω) resistance compared to chemically activated (80 Ω) devices. Similarly, the screen-printed pattern (Figure 4e) showed a similar trend with resistivity of 2.92 mΩ cm for mechanical activation and 4.63 mΩ cm for flux activated. Flux activation, however, better preserves the printed patterns after activation whereas mechanical triggering can lead to shape-edge distortions. Besides the use of a 2D plotter like the Silhouette craft cutter (Figure 2n) or screen printing, the formulated inks were also deposited with a conventional desktop inkjet printer (HP Deskjet 6540) on different materials (e.g., cardboard, kapton tape, glass; Figure S5, Supporting Information). The inkjet printer allows higher resolution in the control of line thicknesses (Figure S5d, Supporting Information) compared to a 2D plotter or screen-printing. Change of the deposition method, however, does not affect performance.

2.3.1. Stability of Printed Features against Repeated Bending

The printed conductive traces, being thin metallic films, are susceptible to failure especially under repeated high strains on a curved surface. Conductive traces were printed on Neenah card stock paper (width = 0.5 mm, height = ≈10 μm, length = 45 mm, Figure 4g). We evaluated resilience of printed traces to repeated bending by following conductivity with repeated (10 000 cycles) straining (Figure 4h,i,k). In all cases, the conductive traces do not delaminate after repeated bending (Figure 4h,i)—a property we attribute to mechanical bonding on the porous paper surface, but resistance increase over the bending cycles. Film resistance increases with degree of curvature and repeated bending (Figure 4l). This increase in resistance correlates with increase in size of developing cracks—a curvature dependent effect (Figure 4m). We observe that modest bending does not significantly increase resistance of the conductive lines (Figure 4h,i,l) except where the paper is folded onto itself (Figure 4j,l). As the diameter of the curvature approaches zero, resistance significantly increases (Figure 4i). Despite the increase in resistance with bending, the lines are still significantly conductive even when the paper is completely

 © 2019 WILEY-VCH Verlag GmbH & Co. KGaA, Weinheim

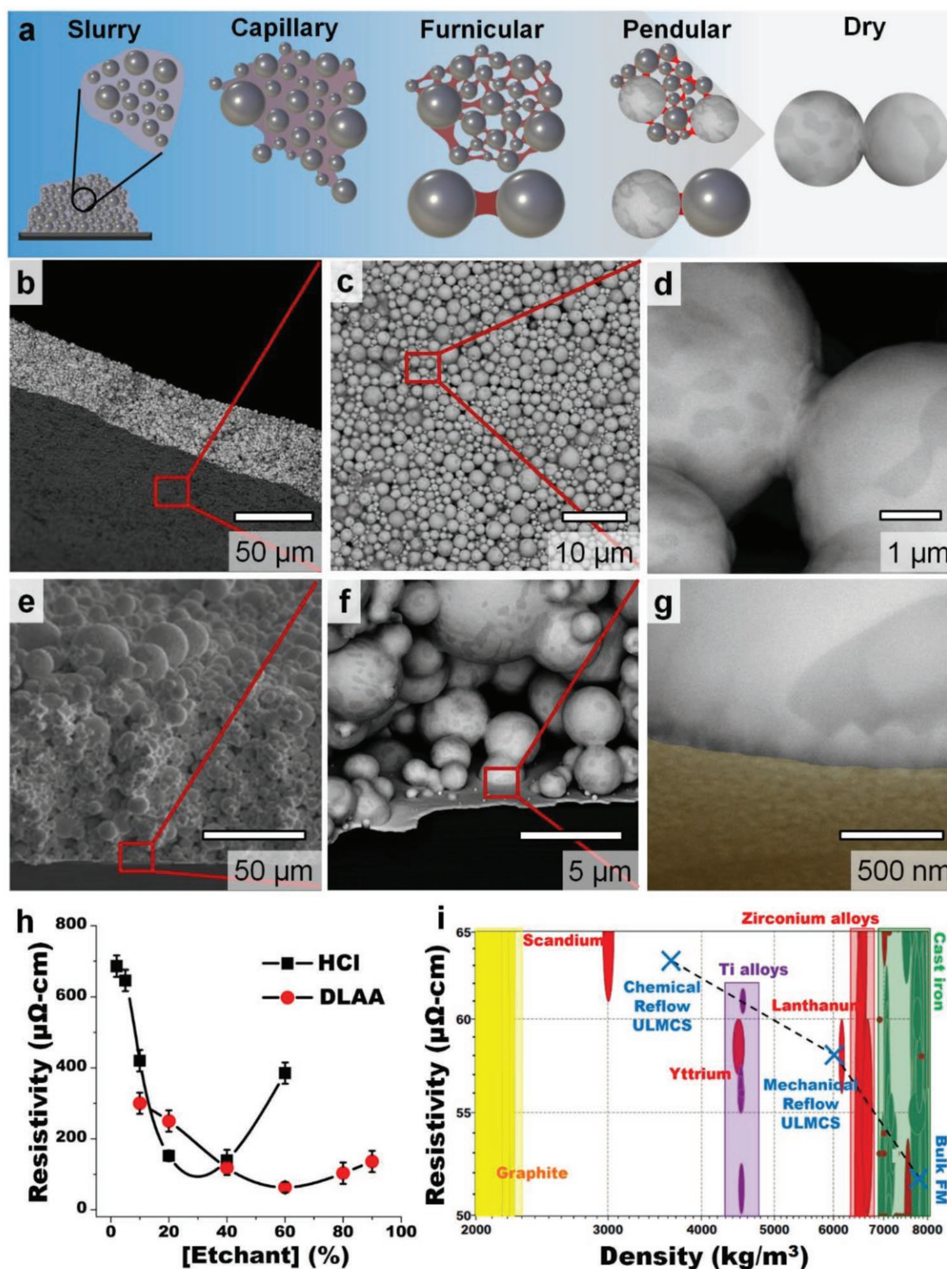

Figure 3. Chemical sintering of ULMCS particles by exploiting capillary driven compaction and self-assembly with concomitant concentration of an etchant at the capillary bridges. a) Illustration of the capillary-driven process from a slurry to evaporative formation of capilary, furnicular, pendular states and eventually the cojoined particles. Localized increased etching at the pendular state leads to sintering and formation of b–d) freestanding films or e–g) surface adsorbed particles with formation of an intermetallic layer at the interface (here between a gold and Field's metal). h) Resistivity of fabricated materials depends on the strength and concentration of the etchant. i) Ashby plot of resistivity versus density illustrates how choice of the activation method affects the specific performance of the produced lines/films.

creased (Figure 4k). We can therefore infer that these conductive traces are applicable to most printed flexible electronics.

2.4. Potential Applications

Having demonstrated the deposition and activation of undercooled particles by exploiting understanding of stress-propagation in both dry and wet colloidal bed, we adopted these methods to fabrication of functional devices.

2.4.1. Surface Mount and Flexible Electronics

To demonstrate versatility of ULMCS particles in surface mount technologies, we prepared a Wheatstone bridge on a regular PCB

© 2019 WILEY-VCH Verlag GmbH & Co. KGaA, Weinheim

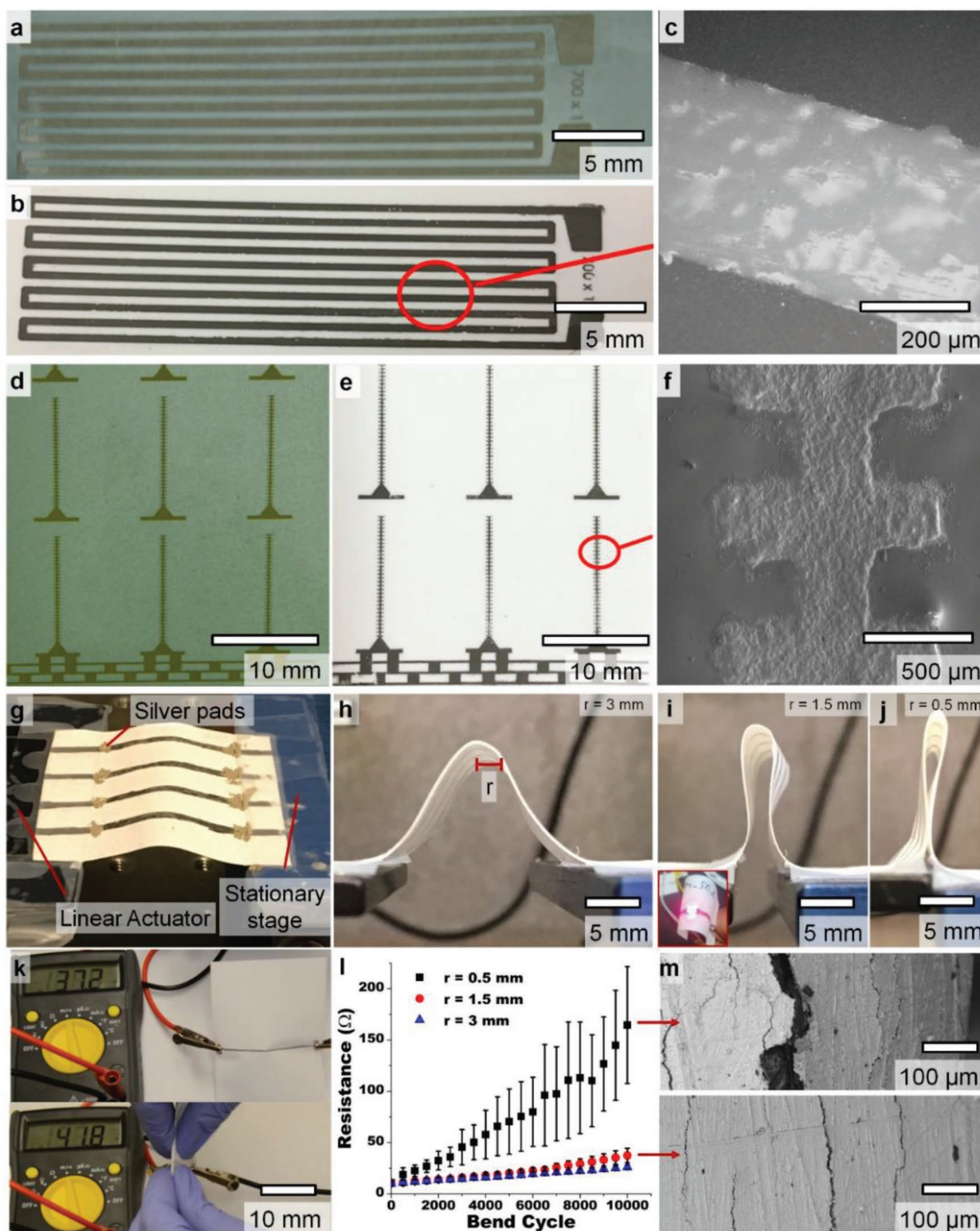

Figure 4. Screen printing and reliability of conductive traces. Screen using with mechanical activation: a) the screen from Novacentrix, b) printed undercooled particles on paper, and c) an SEM close-up view of the printed lines after mechanical sintering. Screen printing with chemical activation: d) the screen from PowerFilm, e) screen-printed undercooled particles on paper, and f) an SEM close-up view of screen-printed lines after CUPACT. Reliability testing under compressive stress: g) bend testing setup, h–j) bending process of paper with radius of curvature ranging from 3 to 0.5 mm (inset: bent paper with LED planted to show continuous conductivity). k) Complete creasing of conductive line and associated increase in resistance. l) Electrical resistance as a function of number of bend cycles of conductive lines on paper. m) Microscopy image of largest defects observed on the printed lines after 10 000 cycles of bending at $r = 0.5$ mm (top) and $r = 1.5$ mm (bottom).

board and on paper (**Figure 5**a,b, Figure S7c–e, and Video S2, Supporting Information). The Wheatstone bridge PCBs were assembled using surface mount resistors using ULMCS particles to create interconnects. As a control, analogous lead-tin solder or conductive adhesive were used. Both ULMCS particles and control devices show comparable performance, that

© 2019 WILEY-VCH Verlag GmbH & Co. KGaA, Weinheim

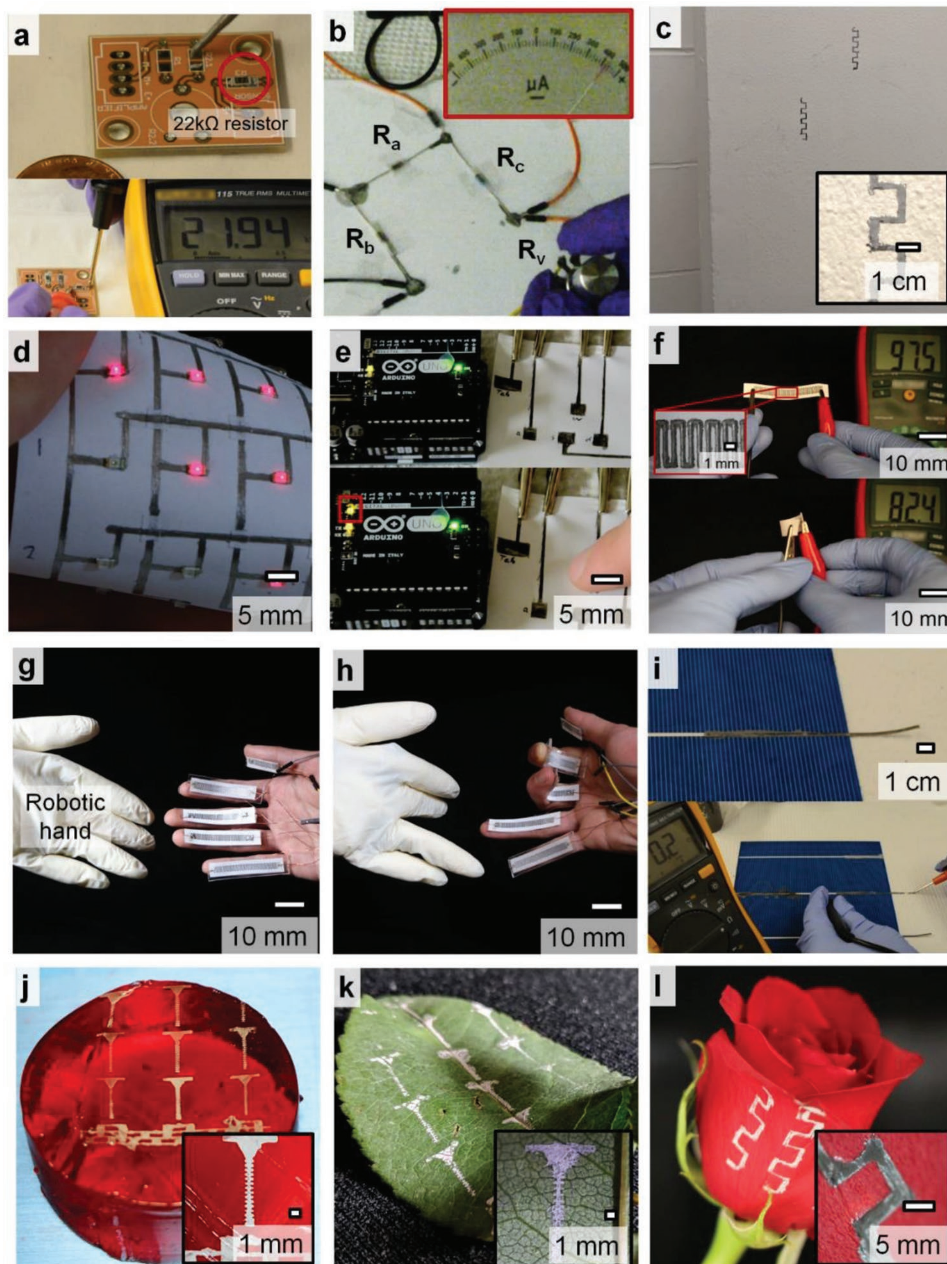

Figure 5. Illustrative examples of applications of ULMCS particles in ambient fabrication: a) mechanochemical soldering of resistors on PCB boards. b) Wheatstone bridge built via CUPACT connections on paper. c) Conductive traces printed on a concrete wall. d) Flexible programmable LED display on a paper substrate. e) Programmable capacitive touch-pad keyboard on paper using ULMCS contacts. f) Flexible variable resistor on paper. g,h) Multiple variable resistor sensors for synchronous controlling/manipulating of a robotic hand. i) Chemically soldered interconnects on a solar cell. j–l) screen-printing on nontraditional complex surfaces: commercial Jello, leaf, and a live rose petal, respectively.

is, give no reading on the galvanometer when the resistance on the bridge matches that on the variable resistor.

Substrate tolerance of the ULMCS particles based inks is confirmed by use of nontraditional substrates like a concrete wall (Figure 5c and Figure S7f, Supporting Information) or a polyethylene grocery bag (Figure S7g,h, Supporting Information). These conductive patterns can potentially serve as a sensors for structural health monitoring[19] or as tamper proof sensors.[20] Exploiting conformal and bend resilience, we applied the undercooled metal ink in fabrication of paper-based Micro-Electro-Mechanical System (MEMS) sensor[16] by manually depositing both the electrical contact (ULMCS particle ink) and the piezoelectric materials (carbon). Performance of the obtained devices was comparable to analogous ones made via screen printing and with a silver contact pad (Figure S7i,j, Supporting Information).[16] Similarly, other paper-based devices like programmable flexible electronic display matrix (Figure 5d), capacitive touchpads (Figure 5e),

© 2019 WILEY-VCH Verlag GmbH & Co. KGaA, Weinheim

and variable resistors (Figure 5f) were fabricated. Interfacing these devices with a microcontroller enables their use as: light up signs, touch keyboards, or in remote control of robotic platforms (Figure 5d–h, Videos S3 and S4, Supporting Information). Drawing wavy lines on paper gives a variable resistor in which resistance tuning is achieved through curvature (Figure 5f and Video S5, Supporting Information). These sensors were printed on a paper and mounted directly on fingers that were then used to remotely control movement of a robotic hand (Figure 5g,h and Video S6, Supporting Information)—a schematic illustration of the circuit layout is given in the Supporting Information (Figure S8a–d).

2.4.2. Solar Cell Devices

Forming electrical contacts on perovskite and amorphous silicon solar cells illustrate compatibility with hybrid or heat sensitive materials (Figure 5i and Figure S8e, Supporting Information). Due to the fragile nature and heat sensitivity of the layered materials, 60% DLAA in ethanol flux was used to create conductive contacts. The flux does not react with the top layer (Phenyl-C61-butyric acid methyl ester, PCBM) of the perovskite solar cell or the top silicon layer of the amorphous silicon device. The resistance of the cells with aluminum contacts (*a*-Si = 14 Ω and perovskite = 30 Ω) is comparable to that derived from our ink contacts (*a*-Si = 18 Ω and perovskite = 35 Ω).

2.4.3. Soft Materials beyond Flexible Substrates

Beside differences in modulus and processing temperature, interfacial surface energy mismatch renders solid metals incompatible with most organic and low surface energy substrates. The shell surface in ULMCS particles, however, present moieties capable of forming favorable secondary interactions with significantly low surface energy substrates compared to the bulk metal. We demonstrate the potential utility of CUPACT to create conductive traces on very soft (low elastic modulus) substrates irrespective of surface energy. We successfully screen printed conductive traces on a soft hydrophilic (Jello) surface (Figure 5j and Figure S8f, Supporting Information), and activated the traces using CUPACT. Similarly, we fabricated conductive traces on a hydrophobic fresh leaf (Figure 5k) and super-hydrophobic rose petals (Figure 5l and Figure S8g, Supporting Information). Since screen-printing requires low applied stress, when paired with CUPACT, it can be used to create conductive lines on readily deformable substrates like Jello, a good analog for soft tissues like the brain. Likewise, CUPACT was used to maintain the integrity of biological materials (e.g., leaves and flowers).

3. Conclusion

In conclusion, we have demonstrated the use of metastable ULMCS particles for ambient heat-free fabrication of metal-based conductive electrical interconnects. Multiple heat-free application pathways highlight the versatility of this approach, allowing a multitude of conductive products to be fabricated without damaging the base material. Furthermore, asymmetric bonding of the particles allows control over porosity, hence, conductivity of the material. We demonstrate unprecedented adaptability of undercooled metal to materials with different compliances, roughness, and surface energies.

4. Experimental Section

Materials: Field's metal (eutectic indium (51%)–bismuth (32.5%)–tin (16.5%)) was purchased from Rotometals. Glacial acetic acid (99.7%), ethyl acetate (99.9%), and hydroxyethyl cellulose were from Fisher Scientific. Diethylene glycol (99.9%) was purchased from VWR.

Undercooled Particles Synthesis: Undercooled metal particles made from Field's metal (eutectic bismuth, indium, tin alloy, Bi:In:Sn = 32.5:51.0:16.5 wt%) were synthesized following the SLICE method.[9b] 1 mL glacial acetic acid was mixed into 200 mL of Diethylene glycol in a graduated cylinder. A commercial soup maker (Cuisinart SBC-1000) was used for the shearing process. Diethylene glycol solution was transferred into the soup maker and heated up to 110 °C, Field's metal pellet was then added and equilibrated for 2 min. The hot mixture of metal and DEG solution was sheared for 30 min at ≈25 000 rpm. The slurry was cooled to ambient, then filtered with Whatman GF/F paper filter placed on a Buchner funnel. Filtered particles were washed with copious amounts of ethanol, then stored in ethyl acetate.

Dry Pressing: Die inner chambers were lubricated using a stearic acid solution (2 g of stearic acid in 100 g of ethanol) prior to use. A varying amount of ULMCS particle slurry in ethyl acetate was placed in a stainless-steel dry pressing molds with an inner diameter of 1.25 cm. The carrier fluid was allowed to evaporate, then the press pole was placed and particles were pressed (Carver Inc., Wabash, IN, USA) from one side with a load of ≈1000–1500 psi.

Mechanical Rolling: Two strips of copper plates, with their native oxides, were cleaned using acetone and dried with a stream of nitrogen. These thin copper plates were layered with a masking tape and then a slurry of ULMCS particles placed on the surface of the tape. After the carrier fluid was evaporated, another copper plate was placed on top of the particles. The copper-sandwiched ULMCS particles were pressed by passing through a jeweler's roller. The pressed particles formed a film that readily delaminated from the tapes as a thin shiny foil.

Preparation of Field's Metal Ink for Rollerball Pen: Carrier fluid was made from a 1:1 mixture of water and methanol. Hydroxyethyl cellulose (HEC) (2%, 0.02 g mL^{-1}) was dissolved in the carrier fluid while stirring at 70 °C until liquid was transparent. The solution was then cooled to ambient conditions. A 75 wt% metal ink was then created by adding ULMCS particles to the cellulosic solution (1:4 w/w cellulose to Field's metal). The dispersion was homogenized using a vortex mixer (Fisher brand).

Preparation of Rollerball Pen: Gelly Roll Metallic pens (Sakura, Inc.) were used for this study. The pen was cleaned by separating its components (barrel, tip, and ball) and washing them with ethanol. The pen was then reassembled and the ink barrel filled with ethanol followed by repeated writing to ascertain that no ink is left in the pen. After draining all the ethanol, the prepared Field's metal ink was loaded into the ink barrel. The reconstituted pen was then used to deposit ULMCS particles.

Screen Printing: As an illustration, screen printing was described on paper. Screens were obtained from Powerfilm and Novacentrix. A sheet of paper was placed under the screen and pressed onto a flat solid surface. Field's metal ink was deposited on screens, then pressed through the screen using a rubber squeegee (Video S1, Supporting Information).

Chemical Sintering: A piece of tape (≈40 µm thickness) was placed on the glass slide and a small channel was cut off from the middle of the tape. Particles were deposited using pipette into the channel and then swiped off using a razor blade to create uniform thickness (≈40 µm).

 © 2019 WILEY-VCH Verlag GmbH & Co. KGaA, Weinheim

Chemical fluxes were made using various concentrations of an acid, ethanol, and a small amount of water. This flux was then applied on the particle films followed by drying under ambient conditions.

Supporting Information

Supporting Information is available from the Wiley Online Library or from the author.

Acknowledgements

This work was supported by startup funds from Iowa State University, a Black & Veatch faculty fellowship, and NSF-SBIR award # 161910. A.M. and Z.M. were partially supported through an Iowa Economic Development Agency summer internship.

Conflict of Interest

M.T. and I.T. hold equity in SAFI-Tech Inc., a company that sells undercooled liquid metal particles analogous to those reported in the manuscript.

Keywords

heat-free solder, interconnects, liquid metal, multimaterial manufacturing, undercooled

Received: May 8, 2019
Revised: June 26, 2019
Published online: July 15, 2019

[1] a) B. Chen, H. Wu, C. Xin, D. Dai, L. Tong, *Nat. Commun.* **2017**, *8*, 20; b) C. Lee, Y. Oh, I. S. Yoon, S. H. Kim, B.-K. Ju, J.-M. Hong, *Sci. Rep.* **2018**, *8*, 2763; c) C. Zhang, C.-L. Zou, Y. Zhao, C.-H. Dong, C. Wei, H. Wang, Y. Liu, G.-C. Guo, J. Yao, Y. S. Zhao, *Sci. Adv.* **2015**, *1*, e1500257; d) M. Sokoluk, C. Cao, S. Pan, X. Li, *Nat. Commun.* **2019**, *10*, 98.

[2] a) J. P. Koppes, K. A. Grossklaus, A. R. Muza, R. R. Revur, S. Sengupta, A. Rae, E. A. Stach, C. A. Handwerker, *Mater. Sci. Eng., B* **2012**, *177*, 197; b) W. H. Qi, M. P. Wang, *Mater. Chem. Phys.* **2004**, *88*, 280.

[3] a) L. Hou, H. Zhao, Y. Lu, *J. Mater. Sci.: Mater. Electron.* **2017**, *28*, 4219; b) M. Santhiago, M. Strauss, M. P. Pereira, A. S. Chagas, C. C. B. Bufon, *ACS Appl. Mater. Interfaces* **2017**, *9*, 11959; c) A. Russo, B. Y. Ahn, J. J. Adams, E. B. Duoss, J. T. Bernhard, J. A. Lewis, *Adv. Mater.* **2011**, *23*, 3426; d) E. C. Garnett, W. Cai, J. J. Cha, F. Mahmood, S. T. Connor, M. Greyson Christoforo, Y. Cui, M. D. McGehee, M. L. Brongersma, *Nat. Mater.* **2012**, *11*, 241.

[4] a) Y. Lu, J. Y. Huang, C. Wang, S. Sun, J. Lou, *Nat. Nanotechnol.* **2010**, *5*, 218; b) D. V. Wagle, G. A. Baker, *Mater. Horiz.* **2015**, *2*, 157; c) G. S. Ferguson, M. K. Chaudhury, G. B. Sigal, G. M. Whitesides, *Science* **1991**, *253*, 776.

[5] a) F. Gao, S. Mukherjee, Q. Cui, Z. Gu, *J. Phys. Chem. C* **2009**, *113*, 9546; b) Y. Peng, T. Cullis, B. Inkson, *Nano Lett.* **2009**, *9*, 91.

[6] L. Liu, H. Huang, A. Hu, G. Zou, L. Quintino, Y. Zhou, *Nano-Micro Lett.* **2013**, *5*, 88.

[7] a) J. Li, W. Gao, R. Dong, A. Pei, S. Sattayasamitsathit, J. Wang, *Nat. Commun.* **2014**, *5*, 5026; b) Q. Wang, W. Han, Y. Wang, M. Lu, L. Dong, *Microsyst. Nanoeng.* **2018**, *4*, 31.

[8] a) M. D. Dickey, *Adv. Mater.* **2017**, *29*, 1606425; b) M. D. Dickey, R. C. Chiechi, R. J. Larsen, E. A. Weiss, D. A. Weitz, G. M. Whitesides, *Adv. Funct. Mater.* **2008**, *18*, 1097; c) R. K. Kramer, C. Majidi, R. J. Wood, *Adv. Funct. Mater.* **2013**, *23*, 5292.

[9] a) S. Çınar, I. D. Tevis, J. Chen, M. Thuo, *Sci. Rep.* **2016**, *6*, 21864; b) I. D. Tevis, L. B. Newcomb, M. Thuo, *Langmuir* **2014**, *30*, 14308.

[10] a) L. Cademartiri, M. M. Thuo, C. A. Nijhuis, W. F. Reus, S. Tricard, J. R. Barber, R. N. S. Sodhi, P. Brodersen, C. Kim, R. C. Chiechi, G. M. Whitesides, *J. Phys. Chem. C* **2012**, *116*, 10848; b) Z. J. Farrell, C. Tabor, *Langmuir* **2018**, *34*, 234; c) R. N. S. Sodhi, P. Brodersen, L. Cademartiri, M. M. Thuo, C. A. Nijhuis, *Surf. Interface Anal.* **2017**, *49*, 1309; d) J. Cutinho, B. S. Chang, S. Oyola-Reynoso, J. Chen, S. S. Akhter, I. D. Tevis, N. J. Bello, A. Martin, M. C. Foster, M. M. Thuo, *ACS Nano* **2018**, *12*, 4744.

[11] a) B. S. Chang, M. Fratzl, A. F. Boyer, A. Martin, H. C. Ahrenholtz, I. De Moraes, J.-F. Bloch, N. Dempsey, M. M. Thuo, *Ind. Eng. Chem. Res.* **2019**, *58*, 4137; b) B. S. Chang, R. Tutika, J. Cutinho, S. Oyola-Reynoso, J. Chen, M. D. Bartlett, M. M. Thuo, *Mater. Horiz.* **2018**, *5*, 416.

[12] J. J. Frenkel, *J. Phys.* **1945**, *9*, 385.

[13] R. K. Bordia, G. W. Scherer, *Acta Metall.* **1988**, *36*, 2393.

[14] a) G. W. Scherer, T. Garino, *J. Am. Ceram. Soc.* **1985**, *68*, 216; b) A. Jagota, C. Y. Hui, *Mech. Mater.* **1990**, *9*, 107.

[15] a) A. H. Clark, L. Kondic, R. P. Behringer, *Phys. Rev. Lett.* **2012**, *109*, 238302; b) A. H. Clark, A. J. Petersen, L. Kondic, R. P. Behringer, *Phys. Rev. Lett.* **2015**, *114*, 144502.

[16] X. Liu, M. Mwangi, X. Li, M. O'Brien, G. M. Whitesides, *Lab Chip* **2011**, *11*, 2189.

[17] I. Buttinoni, J. Cha, W.-H. Lin, S. Job, C. Daraio, L. Isa, *Proc. Natl. Acad. Sci. USA* **2017**, *114*, 12150.

[18] J. S. Marshall, *Phys. Fluids* **2011**, *23*, 013305.

[19] a) I. Kang, M. J. Schulz, J. H. Kim, V. Shanov, D. Shi, *Smart Mater. Struct.* **2006**, *15*, 737; b) G. N. Kawchuk, J. Hartvigsen, T. Edgecombe, N. Prasad, J. H. van Dieen, *Sci. Rep.* **2016**, *6*, 22974.

[20] E. J. Campbell, S. K. Czaplewski, J. Kuczynski, T. J. Tofil, J. T. Wertz, J. Zhang (International Business Machines Corp), *US9859226B1*, **2016**.

© 2019 WILEY-VCH Verlag GmbH & Co. KGaA, Weinheim